Annals of Glaciology



Article

Cite this article: Schild KM, Vaňková I, Sutherland DA, Nicholls K (2024). Deriving iceberg ablation rates using an on-iceberg autonomous phase-sensitive radar (ApRES). *Annals of Glaciology* **65**, e34, 1–7. https://doi.org/10.1017/aog.2024.35

Received: 1 March 2024
Revised: 9 July 2024
Accepted: 11 July 2024

Keywords:
icebergs; melt-basal; radio-echo sounding

Corresponding author:
Kristin M. Schild;
Email: kristin.schild@maine.edu

© The Author(s), 2024. Published by Cambridge University Press on behalf of International Glaciological Society. This is an Open Access article, distributed under the terms of the Creative Commons Attribution licence (http://creativecommons.org/licenses/by/4.0/), which permits unrestricted re-use, distribution and reproduction, provided the original article is properly cited.

cambridge.org/aog

Deriving iceberg ablation rates using an on-iceberg autonomous phase-sensitive radar (ApRES)

Kristin M. Schild[1,2], Irena Vaňková[3], David A. Sutherland[4] and Keith Nicholls[5]

[1]School of Earth and Climate Sciences, University of Maine, Orono, ME, USA; [2]Climate Change Institute, University of Maine, Orono, ME, USA; [3]Los Alamos National Laboratory, Los Alamos, NM, USA; [4]Department of Earth Sciences, University of Oregon, Eugene, OR, USA and [5]British Antarctic Survey, Cambridge, UK

Abstract

The increase in iceberg discharge into the polar oceans highlights the importance of understanding how quickly icebergs are deteriorating and where the resulting freshwater injection is occurring. Recent advances in quantifying iceberg deterioration through combinations of modeling, remote sensing and direct in situ measurements have successfully calculated overall ablation rates, and surface and sidewall ablation; however, in situ measurements of basal melt rates have been difficult to obtain. Radar has successfully measured iceberg thickness, but repeat measurements, which would capture a change in iceberg thickness with time, have not yet been collected. Here we test the applicability of using an on-iceberg autonomous phase-sensitive radar (ApRES) to quantify basal ablation rates of a large (~800 m long) non-tabular Arctic iceberg during an intensive 2019 summer field campaign in Sermilik Fjord, southeast Greenland. We find that ApRES can be used to measure basal ablation even over a short deployment period (10 d), and also provide a lower bound on sidewall melt. This study fills a critical gap in iceberg research and pushes the limits of field instrumentation.

Introduction

The increasing solid ice discharge from tidewater glaciers, and subsequent increase in iceberg abundance, emphasizes the importance of constraining the impact of freshwater flux from transient icebergs on fjord and ocean environments (Cenedese and Straneo, 2023). Previous iceberg ablation studies have focused on calculating and constraining overall mass loss rates (i.e. Russell-Head, 1980; Bigg and others, 1997; Savage, 2001; Enderlin and Hamilton, 2014; FitzMaurice and others, 2017; Moyer and others, 2019) as well as mass loss with depth down the iceberg sidewalls (e.g. Moon and others, 2018; Schild and others, 2021) using a suite of remote sensing, in situ measurements, empirical parameterizations, and numerical modeling approaches. Results from applying an empirical melt rate formulae to Greenlandic icebergs suggest that meltwater from the bottom of an iceberg may remain at depth in the water column, impacting fjord circulation and nutrient transport (Moon and others, 2018; Hopwood and others, 2019). Yet, due to the limitations of remote sensing and current in situ repeat measurements (e.g. multibeam sonar), validation using in situ measurements of basal ablation remains elusive. However, preliminary radar surveys have demonstrated the utility of radar in iceberg-ocean environments. Both fixed-frequency and broad-band impulse radars have successfully captured iceberg thickness and the basal ice-ocean interface of tabular icebergs in Antarctica (Smith, 1972; Kovacs, 1978; Swithinbank, 1978), as well as ice islands (Kovacs, 1978) and irregularly shaped icebergs (Rossiter and Gustajtis, 1978) in the Arctic. While prior applications have focused on capturing single iceberg thickness measurements, more recently, repeat measurements have derived basal melt rates of ice islands using stationary impulse radar (Crawford and others, 2020; Mingo and others, 2020) and melt rates of ice shelves using ApRES (autonomous phase-sensitive radio echo sounding) (e.g. Marsh and others, 2016; Stewart and others, 2019; Vaňková and others, 2021a). In principle, repeat radar measurements could also be used on icebergs to derive basal ablation rates. In this study, we test the applicability of using an on-iceberg, continuously operating, ApRES to capture iceberg basal ablation over a short temporal period (10 d) of a non-tabular (i.e. having rotated at calving) Greenland iceberg.

ApRES is a ground-based, low-power, light-weight, phase-sensitive radar, that is designed to operate autonomously for extended time periods on daily to seasonal, or even inter-annual, time periods. The system was originally designed for capturing basal melt rates of ice shelves possessing smooth, flat ice bases, over spatial scales of the ice thickness (e.g. Nicholls and others, 2015), and has consistently worked well at large Antarctic ice shelves with these properties (e.g. Vaňková and Nicholls, 2022). However, more recently ApRES has also been used to identify ice fabric (e.g. Jordan and others, 2020), firn layers and compaction (Bagshaw and others, 2018; Case and Kingslake, 2021), and to derive basal melting of ice shelves with complex basal geometry (Vaňková and others, 2021a). The continued success of ApRES in identifying small-scale changes (mm) across large ice thicknesses (100 s m) in variable polar

https://doi.org/10.1017/aog.2024.35 Published online by Cambridge University Press

environments, supports its potential capability to capture basal ablation of Arctic icebergs, although some new challenges related to size, geometry, and roughness of the iceberg surface may arise. In this study, we use drone and multibeam surveys to establish the comparative iceberg geometry dataset, and evaluate the ability of ApRES to capture basal ablation of a non-tabular iceberg. Here we outline important considerations for successfully utilizing ApRES, with a strong focus on interpretation of results, identifying successes and shortcomings of using ApRES in this environment, and recommendations for future endeavors. In being able to better constrain basal ablation, we can better inform iceberg deterioration models and begin to quantify the impact of icebergs on ecosystems, fjord stratification, and fjord circulation.

Methods

Field location

To optimize the likelihood of a successful test of ApRES performance, primary considerations in site selection focused on choosing a stable iceberg to instrument and minimizing confounding variables (complete mitigation strategies are individually outlined in Table S1). Ideally, the iceberg would remain upright without any catastrophic deterioration over the deployment period (no loss of instrumentation), and would be large enough to safely deploy and recover instrumentation via helicopter. To facilitate data analysis and validation, a simple surface and sidewall geometry (to aid sidewall return identification) was desirable. Iceberg SF0419, in Sermilik Fjord, southeast Greenland was chosen due to its large size (800 m × 700 m), rectangular shape and minimal signs of tipping (Fig. S1). Iceberg SF0419 was also located at an ideal location in the ~80 km fjord (just outside the mélange; Fig. 1a, black box), decreasing the possibility of the instrumented iceberg transiting out of the fjord during surveying, and enabling ship-based data collection.

Field deployment

Modifications to the ApRES installation addressed constraints of the helicopter (small passenger bay), the limited installation time window (<15 min), and on-iceberg conditions (surface sliding and/or instrument tilt during surface melt or iceberg tipping). Due to the short installation window, traditional subsurface installation was not feasible, and the deployment plan focused on minimizing the influence of surface conditions having the potential to impact measurements. Modifications included affixing wooden 2 × 2 s to each antenna leg to reduce the impact of surface melt and melt-in of the antennas; anchoring the antennas to the iceberg using ice screws and climbing slings to minimize displacement in case of iceberg tilting; and finally, positioning the system on a ridge to channel surface meltwater away from the unit. Iceberg SF0419 was accessed by an Airbus AS350B3e helicopter, with deployment on 27 July 2019 (day of year 208) and recovery 10 d later (5 August 2019, day of year 217). Tandem GNSS units were also deployed on either side of the ApRES (Fig. 1b) to enable more accurate processing of the ship-based multibeam data, and an off-center ApRES deployment (i.e. variable distances to each sidewall) was attempted to minimize competing return signals from the sidewalls and iceberg base.

ApRES settings and data processing

ApRES detects the evolving position of subsurface reflectors by repeatedly transmitting an electromagnetic chirp that smoothly ramps between 200 and 400 MHz. The system is able to accurately measure the phase of the reflected signal, leading to millimeter precision in the detection of temporal changes in the reflector positions (Brennan and others, 2014). ApRES provides a point measurement, in that reflections located at equal travel times are integrated, creating a vector sum of all the reflections from a roughly equal range. Downward orientation, and the design of the antennas, aims to direct the highest radar power at nadir, but sometimes bright, off-nadir reflections (i.e. sidewalls) can significantly contribute to, or even dominate, the received signal from a particular range, potentially complicating data interpretation. Here we follow standard methodology to first derive a stack of displacement time series of subsurface reflectors (Stewart, 2018; Vaňková and others, 2020), and then use the time series to calculate melt rates. Deriving the displacement time series consists of cross-correlating the ApRES complex range-domain signal for a range interval of chosen thickness, here 4 m, for each pair of consecutive time shots, here every 5 min. The displacements are then measured in a Lagrangian frame of reference. The total thickness change ($\dot{h}$), is a sum of thickness changes due to basal melting ($\dot{m}_b$), surface melting ($\dot{s}$) and ice strain thinning ($H\dot{\epsilon}$, where H is ice thickness and $\dot{\epsilon}$ vertical strain rate). While firn density and compaction are critical components in deriving Antarctic ice shelf basal melt rates (e.g. Pritchard and others, 2012), firn is not considered in this study as rotating Arctic icebergs lack firn, and their limited lifespan and capacity for capsizing does not support firn development. We calculate melt rates of the freely floating iceberg following Jenkins and others (2006), where $\dot{\epsilon}$ and $\dot{s}$ are estimated from the slope and intercept of a linear fit to vertical velocities, which are calculated from the line-of-sight displacement time series. This involves identifying ranges where reflectors lie at nadir and using those reflectors for the linear fit. The total thickness change, $\dot{h}$, is derived by tracking the basal reflector or its multiple. Finally, the basal melt rate, $\dot{m}_b$, is calculated as

$$\dot{m}_b = \dot{h} - \dot{s} - H\dot{\epsilon}. \quad (1)$$

Given the relatively short record (10 d), and the challenges involved in extracting even time-averaged estimates due to the complexity of the geometry of the iceberg (compared, for example with an Antarctic ice shelf), our focus is exclusively on deriving mean melt rates.

Iceberg geometry

To evaluate the reliability and precision of the ApRES results, we collected independent measurements of iceberg geometry using drone surveys, multibeam surveys, and supporting measurements, including on-iceberg GNSS and conductivity-temperature-depth (CTD) casts adjacent to the iceberg. The above water iceberg DSM (digital surface model) was constructed from drone imagery (DJI Phantom 4+, 118 photos), collected by flying ~150 m above the surface of the iceberg over <10 min period. We applied Structure from Motion (SfM) processing methods to the imagery in Agisoft Metashape Pro software, and created a dense point cloud (~4.5 cm resolution, RMSE ≤ 0.4 m) following the methods of Crawford and others (2018) and Schild and others (2021). To construct the subsurface DSM of the lateral-facing underwater surfaces, we used a multibeam sonar (Reason T50-P), collected during an ~70 min circumnavigation of Iceberg SF0419. Multibeam scans were first corrected for sound speed attenuation using iceberg-adjacent CTD casts (Sea-Bird 25plus CTD sensor), then corrected for iceberg movement during surveying using both on-iceberg GNSS units (Trimble NetR9 receiver, Zephyr Geodetic II antenna; *lat-lon-h*; ≤ ± 3 cm, every 5 min) and ship-based GNSS (following methods of Shah and others, 2019 and Schild and others, 2021). The above and below water DSMs, collected

https://doi.org/10.1017/aog.2024.35 Published online by Cambridge University Press

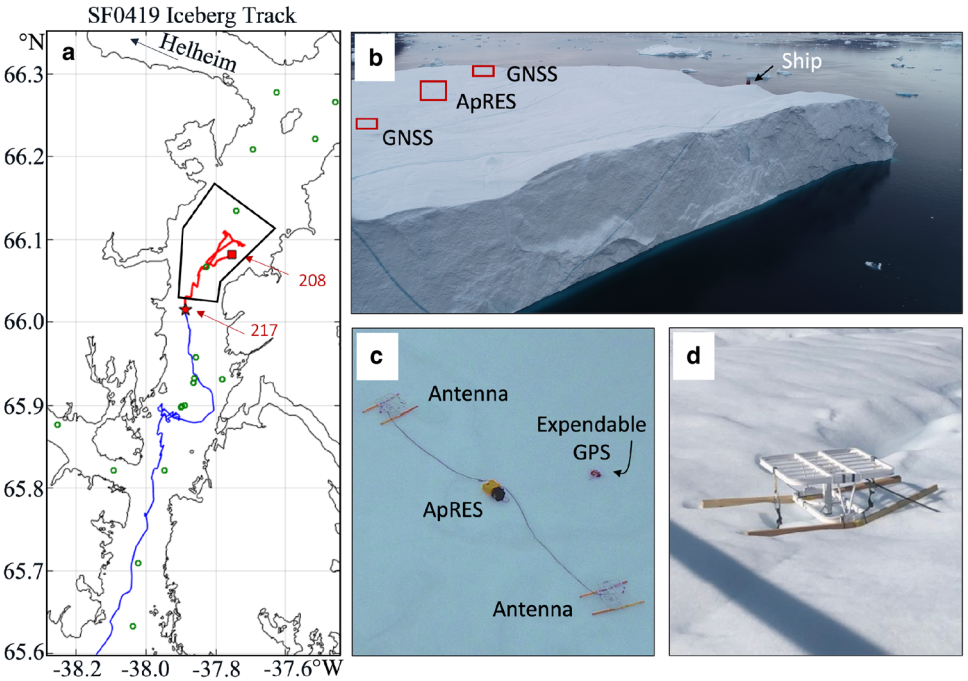


Figure 1. Transit map of Iceberg SF0419 (a), with the ApRES deployment (red square) and recovery (red star) locations and day of year noted, as well as the on-iceberg instrument configuration (b), and modified ApRES antenna configuration after deployment (drone image, c) and at recovery (d). Also noted (a) is the track of the iceberg during ApRES deployment (red line, GNSS), iceberg track post-deployment (blue line, expendable GPS), the identified optimal zone for deployment (black outline), and location of CTD casts (green circles).

sequentially on 30 July (day 211), were aligned using the on-iceberg GNSS and drone imagery. A Poisson reconstruction was applied to the aligned DSMs to close the point cloud (Kazhdan and Hoppe, 2013), creating a 1 m resolution mesh, and accounting for missing data due to obstructions or limitations in the line-of-sight.

Results

Iceberg geometry and behavior

Ship-based measurements of iceberg geometry (drone and multibeam sonar) confirmed a 'straight wall' sidewall geometry (no submerged foot) with undercut slopes of approximately 3°, 5°, 9° and 23° (Fig. 2). Multibeam surveys showed Iceberg SF0419 had a keel depth of ~383 m and variability in the number, width and depth of vertical channels on each face. The total projected volume (using an ice density of 917 kg m^{-3} and in situ average ocean properties from iceberg-adjacent CTD casts) was 1.0×10^8 m^3, with a surface area of 1.37×10^6 m^2 (using the Poisson closed mesh geometry). Over the 10 d deployment period, Iceberg SF0419 traveled ~45 km, moving both up and down fjord (Fig. 1a, red line), with an average velocity of 0.04 m s^{-1}.

ApRES results and interpretation

The ApRES profiles of return amplitude (Fig. 3a) and time-mean velocity (Fig. 3b) show differences in behavior at 220, 350 and 390 m range. Above ~220 m range, the time-mean velocities are linear with range, and quite scattered in the upper 100 m (Fig. 3b). The displacement time series for this top most section (0–100 m) also features a diurnal signal, whose strength is variable with center frequency. This diurnal signal (similar to that observed by Vaňková and others, 2018) is correlated with temperature variations as recorded by the instrument, and suggests changing electromagnetic properties in the upper part of the ice column (Vaňková and others, 2021b). As we are focused on basal melt rate, analysis of this signal is outside the scope of this study, however it could be used to help understand surface properties. Between 100 and ~220 m range, the reflections originate entirely from the interior of the iceberg (Fig. 4a), as opposed to the iceberg-ocean interface, and provide estimates for the vertical strain rate within the iceberg itself. By applying a linear fit to the velocities in the 100–220 m range, we calculate a strain thinning rate of 0.01 ± 0.02 m d^{-1} and surface melt rate of 0.03 ± 0.01 m d^{-1}.

From ~220 m range, the velocity magnitude begins to increase steadily with increasing range, and is accompanied by a relatively abrupt and sustained increase in return amplitude (Fig. 3, dashed orange line; Fig. 4). This shift in behavior coincides with the appearance of a sidewall in the ApRES view, as confirmed by the iceberg geometry profiles. Although sidewalls function as an off-nadir reflector (i.e. low power return), the high impedance contrast of the iceberg-ocean interface results in the return amplitude overshadowing any internal reflectors from within the ice column. This overshadowing occurs despite the position of the ApRES antennas transmitting the majority of its radar power in the downward-looking direction. In addition to the support lent to this interpretation by the geometric profiles of the iceberg, it is also corroborated by the sustained increase in return amplitude being consistent across the time series (Fig. 4).

Beyond 220 m range, there are two return amplitude increases accompanied by drops in velocity, one at ~350 m and the other at 390 m range (Fig. 3, dashed gray line and solid purple line, respectively). The first of these (at ~350 m range) is an isolated peak, which is not sustained with range (Fig. 3) and is interpreted as a region with accumulated low melt, such as a flat shelf. The iceberg geometry profiles suggest that this depth range coincides with a horizontal surface on the 23° face (Fig. 2, blue arrow). In contrast, the second return amplitude peak, at 390 m, is sustained with increasing range and is interpreted as the basal iceberg-ocean interface. This interpretation is confirmed both by the iceberg

https://doi.org/10.1017/aog.2024.35 Published online by Cambridge University Press

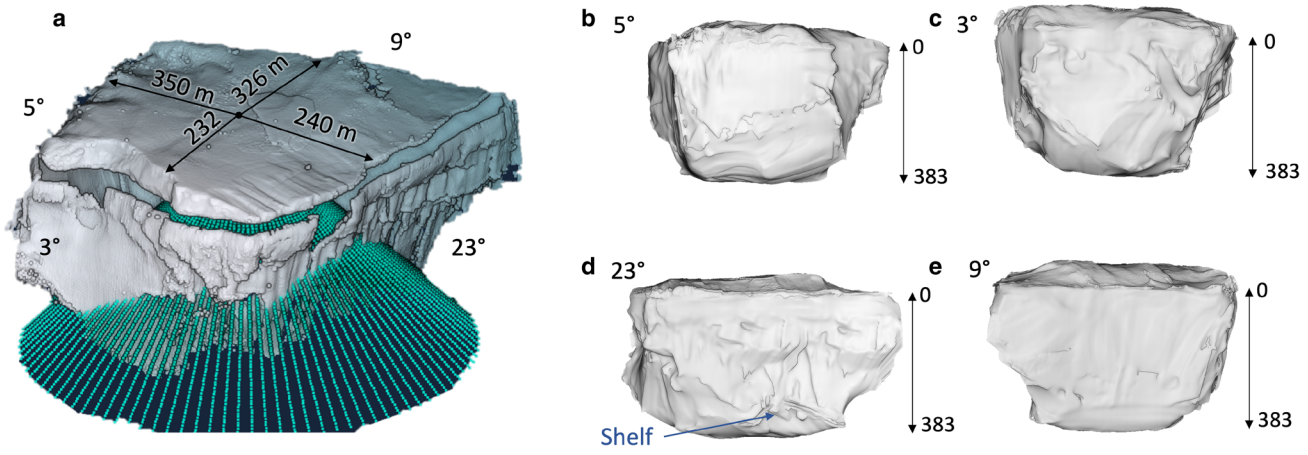


Figure 2. The 3-dimensional drone and multibeam-derived DSM point cloud for Iceberg SF0419 (a), with schematic of ApRES cone (teal dots) and ApRES distance from sidewalls noted. Panels (b–e) show each lateral face of the iceberg, after Poisson reconstruction, with slope and depth noted. Black arrows identify depth below the surface (m), and blue arrow identifies the shelf at ~350 m depth.

geometry profiles and the presence of a 4-way reflection (surface-base-surface-base-surface, first multiple) at ~780 m (Fig. 3a, green line).

To derive basal melt rate, we use Eqn (1), first calculating the total thickness change, $\dot{h}$, by tracking the first multiple of the basal reflection (Fig. 3, green line). We choose the first multiple (Fig. 5b) over the basal reflection (Fig. 5a) as the first multiple is less contaminated by off-nadir (sidewall, low power) returns, and therefore is a clearer and more defined reflection over time, leading to a more accurate thinning rate calculation. Over the 10 d deployment period, we find the iceberg thinned at a mean rate of 0.13 m d^{-1}. In using the calculated strain thinning rate of 0.01 ± 0.02 m d^{-1} and surface melt rate of 0.03 ± 0.01 m d^{-1}, we find a mean basal melt rate of 0.09 ± 0.02 m d^{-1} (Fig. 3b, black cross). In the absence of the first multiple, the basal melt rate derived from the basal reflection could act an upper bound for the basal melt rate as it also would include sidewall melt contributions (Fig. 3b, purple star), however, with multiple returns we are better able to constrain the basal melt rate.

As the ApRES time series also captured sidewall reflections, we next analyzed off-nadir reflections (Fig. 4b) to determine the feasibility of extracting sidewall melt rates. The sidewall reflections

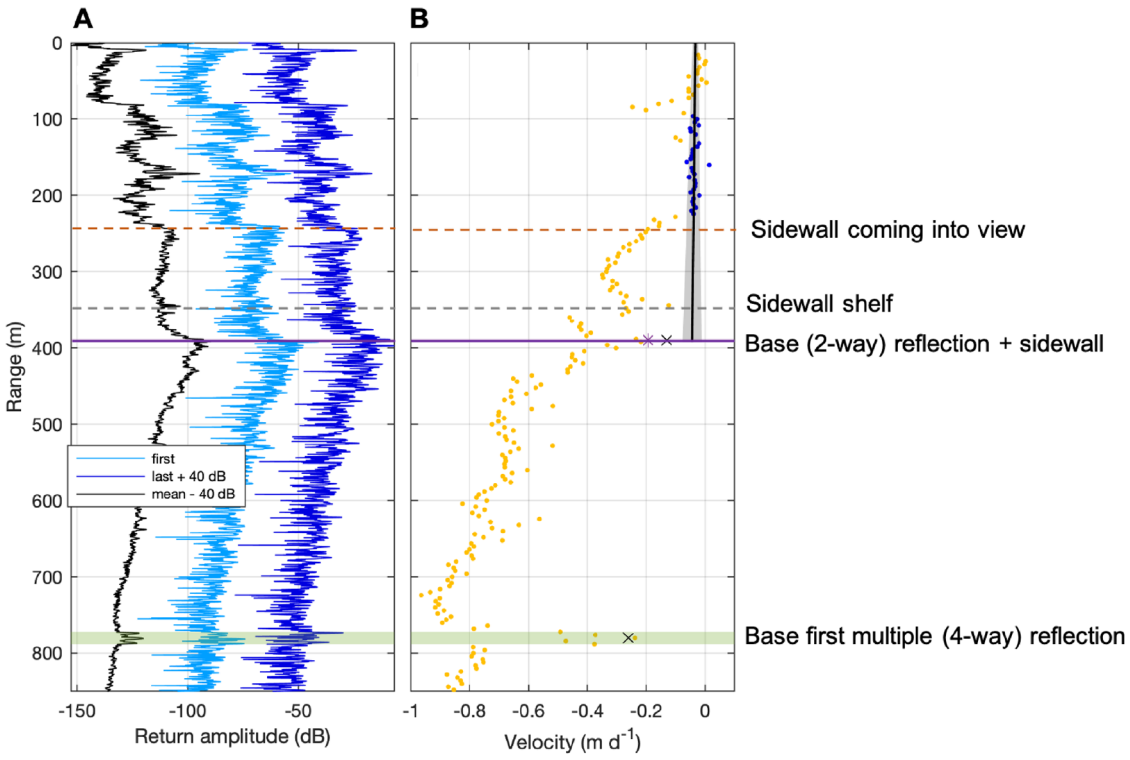


Figure 3. Iceberg SF0419 ApRES range profiles show the return amplitude of the first and last shots, the time-mean return (offset by 40 dB for visibility, a), and mean velocities of each range bin (b, yellow dots), with respect to the ApRES antennas at the iceberg surface (negative velocity is motion toward the antennas). Prominent features of the ApRES profiles are noted, including data used to calculate the vertical strain thinning rate and surface melt rate (blue dots), the basal reflector (purple line) and its multiple (green line), and the visibility of the side wall reflections (dashed orange line) and a prominent ledge (dashed gray line). The line style indicates if the noted feature was identified using a combination of ApRES and iceberg geometry (dashed) or identified solely from ApRES reflections (solid). The thickness of the solid lines represents the range bin thickness used for tracking the respective reflector. The total thinning rate, derived from the basal reflector multiple, (black x on both the base and base multiple ranges) and derived from the first basal reflector (purple star on only the base range) are noted.

https://doi.org/10.1017/aog.2024.35 Published online by Cambridge University Press

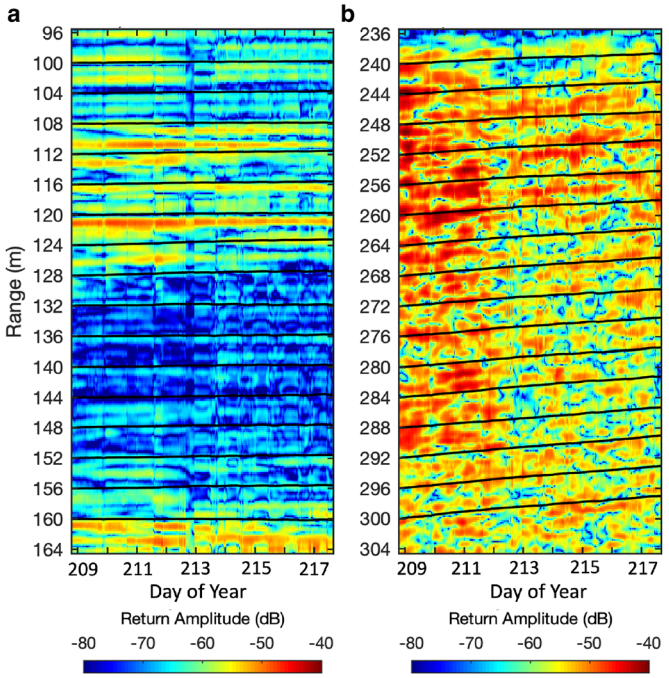


Figure 4. Time series of ApRES return amplitude (dB) with range (m) showing the internal reflections at nadir (a), and the signal dominated by off-nadir reflections from the iceberg sidewalls (b). Solid lines represent the line-of-sight displacement time series, at 4 m range spacing.

are visible past ~220 m range, where the magnitude of negative velocities begins to increase gradually, apart from drops associated with the shelf (~350 m) and the iceberg base (~390 m), stagnating at around ~480 m, and then staying constant until ~560 m (Fig. 3b). In considering the iceberg keel depth (~383 m), the signal past ~560 m is composed exclusively of multiple reflections (e.g. sidewall-to-sidewall-to-surface, or sidewall-to-base-to-surface), and we are therefore not able to disentangle and interpret those returns. However, we can estimate sidewall melt rate using the velocity in the ~480–560 m range, if we assume the following conditions: (1) the sidewall melt rate is higher than the basal melt rate, as evidenced by the larger negative velocities observed above the iceberg base where sidewall reflections dominate in comparison to the actual iceberg base (and supported in laboratory studies by Hester and others, 2021); (2) the sidewall reflection angle from nadir decreases as the range increases, gradually increasing the relative contribution of sidewall reflections to the overall integrated signal; (3) sidewall reflections are the primary factor contributing to the increase in velocity magnitude with range; and (4) melt rates derived from ranges below ~220 m exhibit insufficient depth-based variation to account for the increasing velocity magnitude with range. Given that sidewall returns merge with lower melting returns from horizontal surfaces, any estimation of sidewall melt rate serves as a conservative lower bound on the actual sidewall melting. Therefore, using the stagnating velocities between ~480 and ~560 m serves as the tightest lower bound on the sidewall melt rates and yields a melt rate of ~0.7 m d^{-1}.

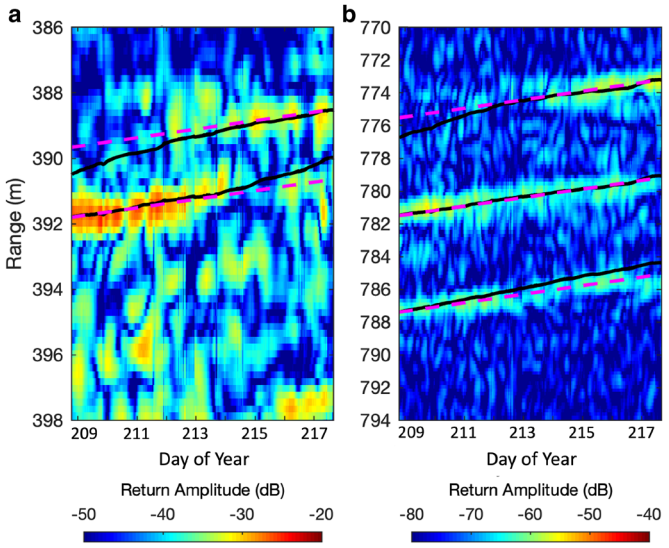


Figure 5. Time series of ApRES return amplitude (dB) with range (m) showing basal (2-way) reflection (a) and first multiple basal (4-way) reflection (b). The dashed magenta line shows a displacement calculated from the mean thinning rate of the 4-way reflection starting near 782 m range, and the black lines show displacement time series derived for each corresponding range segment.

Discussion

Icebergs are extremely challenging to measure as they are actively transiting, rotating, tipping and disintegrating whilst being surveyed. Prior work has demonstrated there is also variability in ablation rate within the same fjord based upon season, distance from glacier terminus (Moyer and others, 2019), transit speed, longevity of survey (Enderlin and Hamilton, 2014; Enderlin and others, 2016; Schild and others, 2021) and the individual iceberg geometry (keel depth; Enderlin and others, 2016; Schild and others, 2021), thereby making accurate and representative calculations of iceberg disintegration challenging to obtain. However, we find that ApRES basal (0.09 ± 0.02 m d^{-1}) and sidewall (~0.7 m d^{-1}) ablation rate estimates agree in magnitude with previous measurements, book-ending average overall ablation rate measurements for a variety of deep-keeled icebergs in Sermilik Fjord (0.1–0.67 m d^{-1}; Enderlin and others, 2016; Schild and others, 2021). Additionally, when using iceberg-adjacent CTD casts, atmospheric conditions and the overall iceberg geometry in an updated set of iceberg melt rate parameterizations (Cenedese and Straneo, 2023), the ApRES measurements overlapped with these modeled basal and sidewall melt rates within the uncertainty bounds (Fig. 6). The agreement between ApRES measurements and these prior ablation studies demonstrates the capacity of ApRES for capturing iceberg ablation rates and underscores its potential inclusion in future research, especially those studies examining melt processes at the ice-ocean interface of large icebergs.

Analysis of the on-iceberg ApRES data presented challenges that diverged from prior ApRES deployments at ice shelves and ice streams. As ApRES was originally conceived to measure basal melt rates of ice shelves at timescales of oceanographic relevance (meso-scale to interannual; Nicholls and others, 2015), the underlying assumptions were that the ice base was smooth, flat, and melting. These ice shelf characteristics then allowed the determination of a Lagrangian thinning rate, where the internal reflecting horizons represented a material surface, in that they were smooth, flat, and stationary with respect to the local ice. These internal reflectors were then used to estimate the strain thinning (or thickening) contribution to the total thinning rate, along with any surface or instrumental effects. However, when applying this method to measure basal melt rate of an iceberg, some key requirements (smooth, flat) are not met if the instrument is placed within range of sidewalls, as will often be the case for non-tabular icebergs. The first challenge in analyzing this dataset was that off-nadir sidewall returns contaminated the basal reflection and skewed the calculated basal melt rates. In this instance, the basal return was only able to provide an upper bound for basal

https://doi.org/10.1017/aog.2024.35 Published online by Cambridge University Press

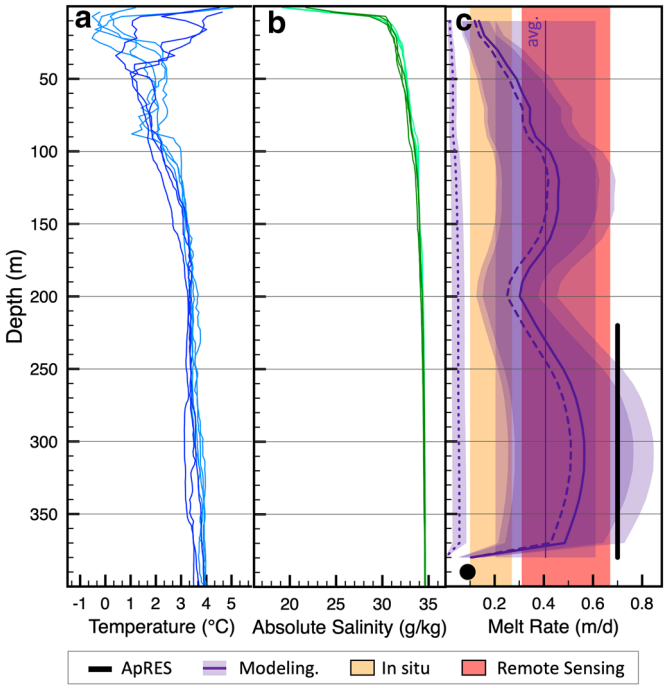


Figure 6. Temperature (°C, a) and absolute salinity ($g\,kg^{-1}$; b) measurements with depth from CTD casts in the north basin of Sermilik Fjord (north of 66°; dark colors are three most adjacent casts; Fig. 1). Also noted are derived iceberg melt rates with depth (c), lower bound from ApRES (sidewall: solid black line, basal: black circle), an updated iceberg melt model from Cenedese and Straneo (2023) (purple lines with shaded uncertainty window of ±50%, average melt: annotated thin line; buoyancy convection: dotted line; forced convection: dashed line; combined buoyancy and forced convection: thick solid line), in situ measurements from Schild and others (2021) (orange box), and remote-sensing calculations from Enderlin and others (2016) (red box). Both in situ and remote-sensing measurements calculated average overall ablation rates, including surface melt, over different periods of time.

melt rate, but we were able to use the first multiple return to calculate what we consider to be a reliable basal melt rate, as other sidewall reflections and reverberations subsided before the arrival of the first multiple. The second challenge was that we were only able to use the relatively narrow 100–220 m range to calculate vertical strain rate (Fig. 3b, blue dots), as the lower half of the ice column was obscured by off-nadir reflections from the sidewalls, and the upper 100 m was affected by evolving electromagnetic properties near the surface. Therefore, most uncertainty in the basal melt rate derivation comes from the strain rate uncertainty. The final challenge in data analysis and interpretation concerned establishing a sidewall melt rate. In analyzing the off-nadir reflections, we assumed that melt rates below 220 m range remained constant to account for the increasing velocity with depth, which was supported by CTD casts, in that if melt rates did increase with depth we would also expect to see changes in the temperature and salinity profiles driving this change in melt (which were not observed, Fig. 6). However, just as the basal signal included sidewall reflections, the off-nadir sidewall returns also included a signal from the lower melting at nadir reflectors (i.e. iceberg base). We therefore present sidewall melt rate as a lower bound to account for this contamination. While this test of ApRES demonstrated its capacity to capture basal melt rates, it also revealed that primary challenges stem from strong off-nadir (sidewall) returns, a characteristic likely common in non-tabular icebergs. In general, the less an iceberg resembles a flat-based ice shelf, the greater the challenge in disentangling reflections and need for additional measurements. Given the complexity of interpreting this iceberg (as compared to ice shelves), smaller or more irregular icebergs than Iceberg SF0419 would likely pose even greater challenges. Therefore, careful consideration of iceberg size and geometry is vital to minimize off-nadir interference in future ApRES applications.

While all efforts were taken during field operations to establish a successful test of on-iceberg ApRES utility (outlined in Table S1), this was a new application and further refinements and updates should be taken into consideration for future Arctic on-iceberg deployments. Our results show that a majority of the modifications to the ApRES on-iceberg instrumental design resulted in a safe and successful deployment, recovery, and data collection campaign. However, surface melt was not adequately accounted for, resulting in the ice screws melting out over the 10 d deployment period and melt water pooling under the antennas (Fig. 1d). Additionally, minimal on-iceberg time did not allow for the collection of a core, so we were not able to conclusively determine temperature, density, porosity, or stratification, which would have helped to better constrain the vertical strain rate calculation. In this test case, knowledge of the geometry of the iceberg, and the location of the ApRES within that geometry, were important for providing confidence in the interpretation of these data. A relaxation of the need for detailed geometry would be realized with the installation of additional ApRES instruments on the iceberg to assist in reducing ambiguities in data interpretation and providing additional confidence in the results.

Conclusions

The increasing abundance of icebergs entering fjords, and the subsequent increase in freshwater injection during melting, can impact fjord circulation, fjord stratification, as well as ecosystem dynamics. However, calculating iceberg ablation rates, specifically the basal melt rate, has been challenging. Previous studies suggest basal freshwater flux may remain at depth (Moon and others, 2018; Hopwood and others, 2019), though observational validation of modeled basal melt rates does not currently exist. In this study, we successfully tested the utility of ApRES on a large (>800 m length) Arctic iceberg in Sermilik Fjord, southeast Greenland, and demonstrated that ApRES can be used to derive basal melt rates, establish a lower bound for sidewall melt rate, and provide some information on iceberg geometry, as long as appropriate care is taken when processing and interpreting return profiles. We found a mean basal melt rate of 0.09 ± 0.02 m d^{-1}, surface melt rate of 0.03 ± 0.009 m d^{-1}, vertical strain rate of 0.01 ± 0.02 m d^{-1}, and using off-nadir returns, an estimated lower bound on sidewall melt rate of 0.7 m d^{-1}. Non-tabular iceberg geometry presents a number of challenges in ApRES data processing and interpretation, in large part, due to the small size of the iceberg in comparison to the extent of an ice stream or ice shelf, and the subsequent contribution of sidewall reflections in the return signal profiles. Therefore, future on-iceberg ApRES deployments will be most successful in targeting large icebergs and/or utilizing supplementary comparison datasets. Overall, this research demonstrates the utility of ApRES for use on an iceberg, while also highlighting that its success was closely tied to iceberg geometry and the availability of complementary in situ measurements to aid in ApRES signal interpretation.

Supplementary material. The supplementary material for this article can be found at https://doi.org/10.1017/aog.2024.35.

Acknowledgements. Support for this work was provided by NASA NIP award 80NSSC21K0945 (K. M. Schild), NSF-OPP CAREER Award 1552232 (D. A. Sutherland), and the Laboratory Directed Research and Development program of Los Alamos National Laboratory under project number 20220812PRD4 (I. Vaňková). Raw on-iceberg GPS positions, full iceberg point clouds (doi: 10.18739/A2KP7TS5N), and raw ApRES data (doi: 10.18739/A2XK84S1W) are available at the Arctic Data Center . The ApRES

processing scripts are available at https://github.com/irenavankova/ApRES_processing. We thank Greenland Copter pilot, Johannes Holst, the Captain and Crew of the R.V. Adolf Jensen, Nicole Abib for assisting in on-iceberg instrument deployment, Dan Duncan for multibeam surveying and raw data processing, and Claudia Cendese and an anonymous reviewer for their helpful and insightful feedback on this manuscript.

References

Bagshaw EA and 9 others (2018) Prototype wireless sensors for monitoring subsurface processes in snow and firn. *Journal of Glaciology* **64**(248), 887–896.

Bigg GR, Wadley MR, Stevens DP and Johnson JA (1997) Modelling the dynamics and thermodynamics of icebergs. *Cold Regions Science and Technology* **26**(2), 113–135.

Brennan PV, Lok LB, Nicholls K and Corr H (2014) Phase-sensitive FMCW radar system for high-precision Antarctic ice shelf profile monitoring. *Sonar Navigation IET Radar* **8**(7), 776–786. doi: 10.1049/iet-rsn.2013.0053

Case E and Kingslake J (2021) Phase-sensitive radar as a tool for measuring firn compaction. *Journal of Glaciology* **68**(267), 1–14. doi: 10.1017/jog.2021.83

Cenedese C and Straneo F (2023) Icebergs melting. *Annual Review of Fluid Mechanics* **55**, 377–402.

Crawford AJ, Mueller D and Joyal G (2018) Surveying drifting icebergs and ice islands: deterioration detection and mass estimation with aerial photogrammetry and laser scanning. *Remote Sensing* **10**(4), 575.

Crawford AJ and 6 others (2020) Ice island thinning: rates and model calibration with *in situ* observations from Baffin Bay, Nunavut. *The Cryosphere* **14**(3), 1067–1081.

Enderlin E and Hamilton G (2014) Estimates of iceberg submarine melting from high-resolution digital elevation models: application to Sermilik Fjord, East Greenland. *Journal of Glaciology* **60**(224), 1084–1092.

Enderlin EM, Hamilton GS, Straneo F and Sutherland DA (2016) Iceberg meltwater fluxes dominate the freshwater budget in Greenland's iceberg-congested glacial fjords. *Geophysical Research Letters* **43**(21), 11–287.

FitzMaurice A, Cenedese C and Straneo F (2017) Nonlinear response of iceberg side melting to ocean currents. *Geophysical Research Letters* **44**(11), 5637–5644.

Hester EW, McConnochie CD, Cenedese C, Couston LA and Vasil G (2021) Aspect ratio affects iceberg melting. *Physical Review Fluids* **6**(2), 023802.

Hopwood MJ and 9 others (2019) Highly variable iron content modulates iceberg-ocean fertilisation and potential carbon export. *Nature Communications* **10**(1), 5261.

Jenkins A, Corr HF, Nicholls KW, Stewart CL and Doake CS (2006) Interactions between ice and ocean observed with phase-sensitive radar near an Antarctic ice-shelf grounding line. *Journal of Glaciology* **52**(178), 325–346.

Jordan TM, Schroeder DM, Elsworth CW and Siegfried MR (2020) Estimation of ice fabric within Whillans Ice Stream using polarimetric phase-sensitive radar sounding. *Annals of Glaciology* **61**(81), 74–83.

Kazhdan M and Hoppe H (2013) Screened Poisson surface reconstruction. *ACM Transactions on Graphics* **32**(3), 1–13.

Kovacs A (1978) Iceberg thickness and crack detection. In *Iceberg Utilization*. Elmsford, NY, USA: Pergamon, pp. 131–145.

Marsh OJ and 6 others (2016) High basal melting forming a channel at the grounding line of Ross Ice Shelf, Antarctica. *Geophysical Research Letters* **43**(1), 250–255.

Mingo L, Flowers GE, Crawford AJ, Mueller DR and Bigelow DG (2020) A stationary impulse-radar system for autonomous deployment in cold and temperate environments. *Annals of Glaciology* **61**(81), 99–107.

Moon T and 5 others (2018) Subsurface iceberg melt key to Greenland fjord freshwater budget. *Nature Geoscience* **11**(1), 49–54.

Moyer A, Sutherland D, Nienow P and Sole A (2019) Seasonal variations in iceberg freshwater flux in Sermilik Fjord, Southeast Greenland from Sentinel-2 imagery. *Geophysical Research Letters* **46**(15), 8903–8912.

Nicholls KW and 5 others (2015) A ground-based radar for measuring vertical strain rates and time-varying basal melt rates in ice sheets and shelves. *Journal of Glaciology* **61**(230), 1079–1087.

Pritchard H and 5 others (2012) Antarctic ice-sheet loss driven by basal melting of ice shelves. *Nature* **484**(7395), 502–505.

Rossiter JR and Gustajtis KA (1978) Iceberg sounding by impulse radar. *Nature* **271**(5640), 48–50.

Russell-Head D (1980) The melting of free-drifting icebergs. *Annals of Glaciology* **1**, 119–122.

Savage S (2001) Aspects of iceberg deterioration and drift. In Balmforth NJ and Provenzale A (eds), *Geomorphological Fluid Mechanics*. Lecture Notes in Physics, vol 582. Berlin, Heidelberg: Springer, pp. 279–318.

Schild KM, Sutherland DA, Elosegui P and Duncan D (2021) Measurements of iceberg melt rates using high-resolution gps and iceberg surface scans. *Geophysical Research Letters* **48**(3), 089765.

Shah V and 7 others (2019) Multi-sensor mapping for low contrast, quasi-dynamic, large objects. *IEEE Robotics and Automation Letters* **5**(2), 470–476.

Smith B (1972) Airborne radio echo sounding of glaciers in the Antarctic peninsula. *British Antarctic Survey Scientific Reports* **72**, 1–11.

Stewart CL (2018) Ice-ocean interactions beneath the north-western Ross Ice Shelf, Antarctica. Thesis. doi: 10.17863/CAM.21483.

Stewart CL, Christoffersen P, Nicholls KW, Williams MJ and Dowdeswell JA (2019) Basal melting of Ross Ice Shelf from solar heat absorption in an ice-front polynya. *Nature Geoscience* **12**(6), 435–440.

Swithinbank C (1978) Remote sensing of iceberg thickness. In Husseiny AA (Ed.), *Iceberg Utilization*. Proceedings of the First International Conference and Workshops on Iceberg Utilization for Fresh Water Production, Weather Modification and Other Applications Held at Iowa State University, Ames, Iowa, USA, October 2–6, 1977. Elmsford, NY, USA: Pergamon, 100–107.

Vaňková I and Nicholls KW (2022) Ocean variability beneath the Filchner-Ronne Ice Shelf inferred from basal melt rate time series. *Journal of Geophysical Research: Oceans* **127**(10), e2022JC018879.

Vaňková I and 5 others (2018) Vertical structure of diurnal englacial hydrology cycle at Helheim Glacier, East Greenland. *Geophysical Research Letters* **45**(16), 8352–8362.

Vaňková I, Nicholls KW, Corr HF, Makinson K and Brennan PV (2020) Observations of tidal melt and vertical strain at the Filchner-Ronne Ice Shelf, Antarctica. *Journal of Geophysical Research: Earth Surface* **125**(1), e2019JF005280.

Vaňková I, Cook S, Winberry JP, Nicholls KW and Galton-Fenzi BK (2021a) Deriving melt rates at a complex ice shelf base using in situ radar: application to Totten Ice Shelf. *Geophysical Research Letters* **48**(7), e2021GL092692.

Vaňková I, Nicholls KW and Corr HF (2021b) The nature of ice intermittently accreted at the base of Ronne Ice Shelf, Antarctica, assessed using phase-sensitive radar. *Journal of Geophysical Research: Oceans* **126**(10), e2021JC017290.

https://doi.org/10.1017/aog.2024.35 Published online by Cambridge University Press